

Sensorized Foam Actuator with Intrinsic Proprioception and Tunable Stiffness Behavior for Soft Robots

Saravana Prashanth Murali Babu,* Francesco Visentin, Ali Sadeghi, Alessio Mondini, Fabian Meder, and Barbara Mazzolai*

Soft robots require actuators with integrated sensing components that perceive unstructured, dynamic environments without compromising their performance. However, many soft robotic systems still rely on external sensors, which affect the functionality, response time, and payload. To overcome these issues, herein a sensorized foam actuator (SFA) with a foam core that acts as both an actuator and a proprioception-sensing element is developed. The integrated modules can sense direct actuation and passive deformation due to extrinsic stresses through a specific pore shape evolution, which leads to a distinct variation in the resistivity pattern. In addition, a fiber-reinforced skin encapsulating the SFA facilitates a fast and efficient response. The SFA is able to lift more than 500 times its own weight with a load-withstanding capacity of 235 N, linear contraction up to 70% strain, and a recovery speed of 13.3 mm s^{-1} . In addition, the SFA is lightweight (34 g), has low hysteresis (<4%), and can self-sense its current deformation state. As proof of concept, various soft robotic applications are presented such as compression piston-like motion, modular inchworm-like crawling locomotion, and a robotic trunk-like manipulation.

1. Introduction

Unlike conventional robots, soft robots are mostly inspired by biological systems and try to imitate the intrinsic softness, flexibility, and adaptability that conventional robots cannot achieve without direct control of motor function.^[1] In conventional robots, the components, such as motors, sensors, rigid links, and controllers, are usually easily stacked. Soft robotics, instead, imitates biological structures in which sensing, control, and actuation are fully integrated and distributed in a soft body.^[2–4] In addition, a soft and flexible body enables the robot to be lighter, adaptable, and operable in human-inhabited environments, where both robustness and reliability ensure compliance and safety.^[5,6]

This approach to robotics has created a series of novel soft mobile platforms, manipulators, and other structures that

perform increasingly complex tasks, such as locomotion on uneven terrain, manipulating objects of known and unknown shapes, wearable robotics—all benefitting from the intrinsic property of a soft robotic system.^[7–10]


There are several actuation principles behind these goals, which span from pressure-driven^[11–13] and tendon-driven^[14,15] to various stimulus responses (e.g., humidity, temperature, light).^[16–19] Of these, pneumatic-driven, soft, muscle-like actuators exploit the effects of multiple mechanical deformations to generate controlled motion.^[20–22]

To better understand the actuation of soft deformations and the related robotic behavior, embedded sensing plays a major role in controlling the current configuration and enabling a live interaction with the environment. An inherently compliant system thus needs to be able to sense whether the deformation is self-induced through actuation or a consequence of an external stimulus. Using such information, a soft actuator can detect changes in the environment and adapt to them by modifying its configuration,^[23] behavior,^[24] and the force applied.^[25] However, in most cases, this information is provided by external sensing units, such as cameras or motion trackers.^[26] Some elastomeric-based actuators have also demonstrated both exteroception and proprioception through embedded strain and pressure sensors,^[27,28] enabling them to sense and respond to external forces.^[29–33]

S. P. Murali Babu
The BioRobotics Institute
Scuola Superiore Sant'Anna
Viale Rinaldo Piaggio 34, Pisa 56025, Italy
E-mail: saravana.murali@iit.it, saravanaprashanth@outlook.com

S. P. Murali Babu, Dr. F. Visentin, Dr. A. Sadeghi, Dr. A. Mondini,
Dr. F. Meder, Dr. B. Mazzolai
Center for Micro-BioRobotics – Bioinspired Soft Robotics Laboratory
Istituto Italiano di Tecnologia
Viale Rinaldo Piaggio 34, Pontedera 56025, Italy
E-mail: barbara.mazzolai@iit.it

Dr. A. Sadeghi
Faculty of Engineering Technology
University of Twente
Horst – Ring 217, Enschede 7500 AE, The Netherlands

 The ORCID identification number(s) for the author(s) of this article can be found under <https://doi.org/10.1002/aisy.202100022>.

© 2021 The Authors. Advanced Intelligent Systems published by Wiley-VCH GmbH. This is an open access article under the terms of the Creative Commons Attribution License, which permits use, distribution and reproduction in any medium, provided the original work is properly cited.

DOI: 10.1002/aisy.202100022

Elastomeric soft machines thus continue to grow in complexity, and roboticists push the boundaries of soft robotics toward more sophisticated designs of actuators and sensors. The most commonly used sensors in soft robots are either surface sensors for pressure and touch detection, or embedded sensors along neutral bending axes to measure the global curvature of the robot limb.^[34,35] These types of sensors are typically integrated to measure a specific type of deformation via changes in resistance or capacitance (e.g., pressure at a certain point or bending along a certain axis), which limits the information that they can give about a robot's configuration.^[36,37] To further reduce the complexity and provide increased functionality, soft robots use intelligent solutions based on smart materials that are capable of both sensing and actuation.

Conductive composites and textiles enable sensing to be embedded within actuators and robots. However, the conductive pigments or polymers are often difficult to process, resulting in brittle coatings that break during deformation with a total loss of or insufficient conductivity, therefore limiting their use.^[38] The chemical combination of conductive polymers and pigments with a substituent or a large organic dopant has improved the functionality of these materials,^[39–41] producing composites that can be embedded into soft devices by enabling integrated sensing, especially as stretchable sensors.^[42]

To fully predict the configuration and behavior of a soft robot, actuators and sensors need to be integrated within a whole structure to actuate and detect arbitrary deformations. However, this design principle should not weaken the actuator's performance; instead, it should enable a robust controlling device to recognize complex configurations without losing functionality, and facilitate the development of human-friendly robots with embedded sensing.^[43,44] Foam actuators are a step further toward simplifying the integration by eliminating the complex design process, extra payload, and need for pneumatic channels and chambers.^[45,46]

Here, we introduce a composite actuator–sensor system with a proprioceptive-like response, which is based on an integrated design of a versatile sensorized foam actuator (SFA). The integrated sensor measures millimeter-scale deformation using relative resistance changes, which are related to the different evolutions of pore deformation by active and passive foam compression. The measurements are used to compute the strain of the actuator during its compression and relaxation motion. The prototypes are obtained by straightforward 2D manufacturing using commercially available materials, resulting in actuators that are soft, yet robust, and intrinsically proprioceptive. The proposed structure provides both active compression and extension. It can lift up to 500 times its own body weight, with a linear compression ratio of $\approx 70\%$, and a hysteresis error lower than 4%.

We also demonstrate its versatile modular integration within more complex configurations based on series and parallel arrangements of SFA modules. Soft modular robots were assembled to perform crawling, manipulate objects with load detection, and pull different loads by a compression piston-like motion. All these examples show the exceptional importance and great potential of using the materials' functionality to reduce complexity, while increasing the performance of soft robotic systems.

2. Results and Discussion

2.1. Deformation and Differentiating Sensing Characteristics of the Foam Core

The conductive foam of the SFA was manufactured by a “dip and squeeze” process in which the polyurethane foam (PU) is soaked in a prepared solution of conductive ink to create a conductive polyurethane foam (cPU) (see Experimental Section and Figure S1, Supporting Information, for an overview of the various steps in the synthesis of the conductive ink and the sensor, and also Video S8, Supporting Information, for a full overview of the straightforward preparation process). Depending on the amount of ink, the total resistivity of the foam changes (1–50 k Ω). Consequently, the results are analyzed and plotted considering the relative resistance change ($\Delta R/R_0$) to provide a direct comparison. To evaluate the mesostructure of both the original, PU, and the modified, cPU, we analyzed the polyurethane foams using various imaging techniques such as optical and scanning electron microscopy (Figure 1A,C), all of which showed the open porous structure before and after the conductive ink coating. The porosity is $\varphi = 0.6$ given by the volume fraction of the porous phase denoted by $\varphi = V_p/V$, where V_p is the volume of the pore phase (the holes) and $V = V_p + V_s$ (volume of the solid phase is V_s).^[47] The calculation based on assumption is shown in Supporting Information 6, Measurement and Data Analysis. The foams were characterized and compared in terms of their stress–strain and the results of the evaluation are shown in Figure 1B,D.

The addition of the carbon-based ink does not significantly influence the stress–strain curve. However, in this configuration the actuator can only be passively deformed when an external force is applied (yellow curves in Figure 1B,D). To actively control the deformation of the conductive foam, we enclosed it within a membrane or skin (Figure 2A). The use of the skin does not compromise the passive compression of the foam when an external force is applied; the skin just extends the actuation functionalities by enabling the use of both positive and negative pressure as the actuation source. When the foams are encapsulated by the skin, the stress–strain results show a substantial difference between the normal and conductive foam (orange curves in Figure 1B,D).

The two actuation modes also show different results (Figure 1E,F). In fact, due to the different effects of the applied forces on the porous structure of the foam, it is possible to differentiate between the behavior of the resistance upon actuation (active compression) or mechanical deformation (passive compression). During passive compression, the force is only applied on either direction of the foam by pushing the structure to partly close the pore walls. In contrast, in active compression (under vacuum @ 90 kPa), the dynamic pore deformation takes place by pulling the pore walls inward from multiple directions, as shown in Figure 1E,F and also Video S1, Supporting Information.

Figure 1G shows images of the pore deformation of the sensorized foam for both cases. When the vacuum is applied, the relative change in the resistivity follows a linear behavior (10–70% of strain) with a steady variation from -3% to -95% . The linear behavior during actuation is suggested to be caused by the homogenous pore deformation and closure due to the

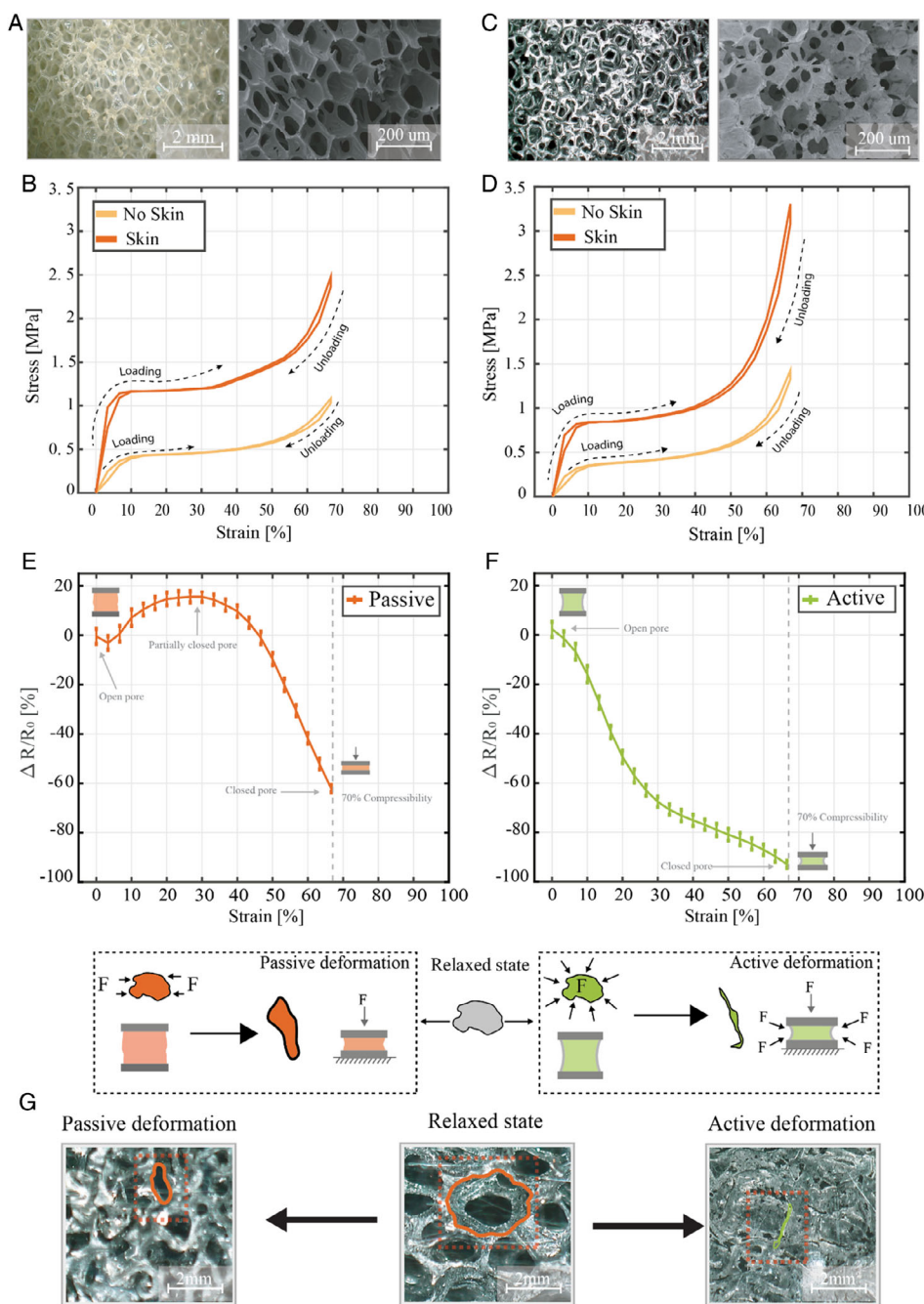


Figure 1. A,C) Optical and scanning electron microscope (SEM) images of the polyurethane foam (PU) and the open porous composite after coating with conductive ink. B,D) Stress–strain behavior of PU foam and conductive PU foam with and without encapsulating fiber-reinforced skin to demonstrate the effect of porosity during mechanical stress by the loading and unloading cycles. E,F) Measured response of the fabricated sensor under one strain cycle with two different modalities of resistance measurements: 1) passive (orange) and 2) active—applied vacuum of -10 kPa (green). The vacuum data exhibited a linear response with a very small hysteresis ($<4\%$) with the maximum strain of 70% . Active and passive actuation exhibited a totally different sensor response enabling the source of deformation to be distinguished and monitored. Illustration of the mechanism of the pore evolution during active and passive deformation. The relative resistance change is different when the pore is unidirectionally compressed by an external mechanical force compared to the multidirectional deformation under vacuum-driven actuation. During passive compression it only partly closes the pores, whereas the active compression by a vacuum homogeneously shrinks the pore, leading to the different change in resistivity. G) Optical images of the sensorized foam showing pore deformation under active and passive compression confirming the mechanism shown in (E,F).

instantaneous behavior by the applied vacuum, whereas in passive compression, first an increasing, quadratic trend of the

relative resistance change in the range of -2% to $+15\%$ is observed ($10\text{--}44\%$ of strain), followed by a linear decrease

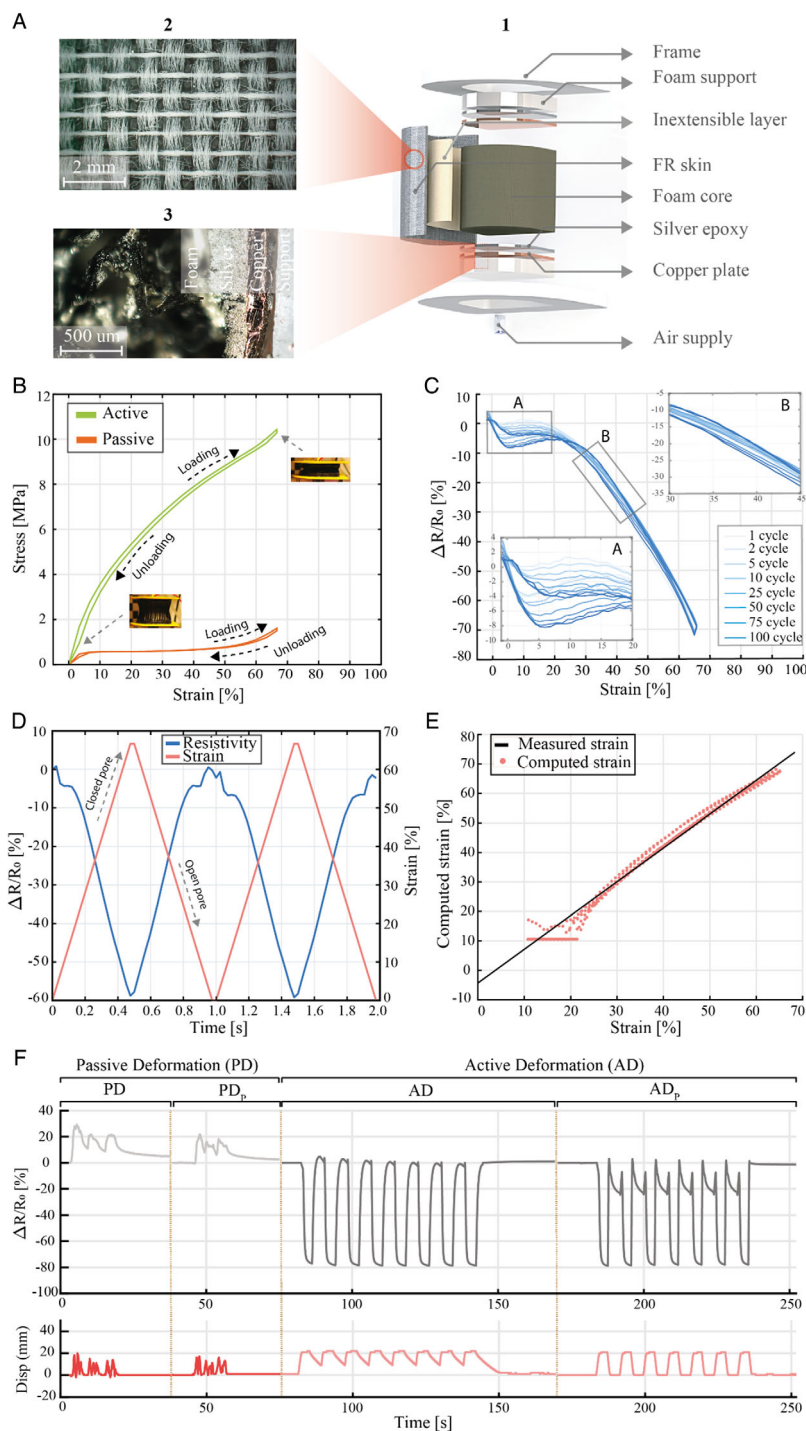


Figure 2. A) Design of the conductive foam actuator in an exploded view (1) with the rapid prototyping method, including all the components used for fabrication. The zoomed-in image on the left (2) shows the alignment of fibers on the skin, sealing the actuator and the cross-section image (3) of the complete actuator with the fabrication layers of the support frame, copper plate, silver epoxy, and conductive foam. B) Stress–strain behavior of the actuator under applied vacuum of -90 kPa. The plot is an average of ten loading and unloading cycles of the actuator. Compared with the passive stress–strain behavior of the cPU foam, the actuator shows a linear behavior compared to the passively deformed conductive foam. C) Resistance change at selected cycles (1–100) and the zoomed-in box “A” exhibiting a large drift in the $\Delta R/R_0$ in the strain interval of 0–20% of the actuator’s deformation, whereas in box “B” a small drift is exhibited in the sensor data with linear characteristic. D) Resistance change and strain profile plotted over time selecting the first two cycles from the experimented data. E) The fitted curve in Figure 2E (blue dots) is plotted using the inverse fitting function shown in Figure S7C,D, Supporting Information, by correlating the actual relative resistance data which are plotted over the strain percentage along the time period. F) Experimental verification to discriminate between passive and active deformation of the actuator with the corresponding tracking of the actuator’s displacement.

between -0.6% and -62% (compression strain from 45% to 70%). This differential variation is likely due to the only partial closing of the porous structure and the quadratic trend is caused by the applied mechanical force. This difference in sensor data estimates the current state of the actuator in both active and passive compression. This significant difference in the signal evolution opens up a new perspective to analyzing and addressing the macroscopic behavior of the pore deformations in the actuator. In fact, as the profiles of the two events are independent, we can clearly differentiate between them, and understand whether the vacuum has been applied.

2.2. Performance and Proprioceptive Behavior of the Actuator

The implementation of the SFA as a device that combines pneumatic actuation with resistive sensing is shown in Figure 2A. The SFA is manufactured in a three-step process: 1) design and wire-cutting of the foam core, 2) sensor integration by “dipping and squeezing” the foam core in conductive ink, and 3) encapsulation of the CPU core within a thin masking layer of paper and a polyethylene-based fiber-reinforced skin. Two rigid supports are then placed at the ends of the foam core.

The components and the assembly of the actuator are shown in Figure 2A. The shape and design of the actuator depend on the application, and some of the most commonly used shapes to construct a soft actuator or device are triangular, ellipse, or rectangular shape as presented in the literature.^[47,48] In this work, we simply chose to use square- and dome-shaped designs while maintaining the volume constant. The setup, as detailed in Figure S4, Supporting Information, is used to characterize the actuator performance in terms of deformation sensing and force exerted.

The SFA can be operated in both negative (compression) and positive pressure (relaxation) conditions. When negative pressure is applied to the internal volume through a supply channel, the entire SFA structure collapses inward. Then when the actuation is turned off, it can return to its initial state thanks to the elastic properties of the foam core. With a positive pressure, the transition between the compressed and relaxed state of the actuator occurs at higher speed (Figure S3 and Video S4, Supporting Information). We tested the actuator with a compressive loading and unloading cycle to characterize its mechanical properties. We performed an average of ten cycles of stress versus strain of the SFA under an applied pressure of -90 kPa, as shown in Figure 2B. The same plot is compared with the stress-strain behavior of the passive actuation, which shows a clear difference in the behavior of the foam core by changes in the stress profile in Figure 1D.

The SFA's behavior was analyzed based on the source of actuation and the strain percentage plotted over the experimental time period. The resistance for the unstrained as-fabricated samples was 200 ± 6.5 k Ω in the relaxed state, and 5 ± 1.2 k Ω in the fully compressed state. To measure the changes in resistance, we connected the actuators in a voltage divider configuration with a reference resistor of 100 k Ω ($<1\%$ accuracy) to sense the dynamic deformations of the actuator with a real-time response and millisecond resolution.

Figure 2C shows the relative drop in resistance with increasing compression strains under deformation at a travelling speed

of 30 mm min⁻¹. The sensor maintains the same strain profile data for a minimum of 100 cycles of compression/relaxation from 0% to 70% by correlating with the relative resistance variation. As shown in the figure, the resistance almost completely recovers after releasing it from a 70% compression strain. This means that the sensor response with active compression has an expected strong correlation between the relative resistance and applied compression strain, as shown in Figure 2D. The SFAs are robust and reliable in terms of actuation and sensing as confirmed in long-term experiments for more than 10 000 cycles, as shown in Figure S7B, Supporting Information.

Figure S6A, Supporting Information, shows the quadratic variation in $\Delta R/R_0$ up to 45% of strain due to the closing or opening of the porous structure, which follows the same trend in Figure 1E. In fact, when the active compression is used, there is still a negative slope, but the concavity is positive.

To better demonstrate this behavior, a section of the graph is highlighted in Figure 2C, where “A” and “B” are close-ups of the plots. The change in $\Delta R/R_0$ that occurred during active compression starts from -2.07% to -69.09% corresponding to the strain percentage of 10% and 70%, respectively. Similarly, for passive compression, the change begins from -9.07% to -37.31% taken at the same strain percentage of 10% and 70% (see Figure S6A, Supporting Information). The evolution of pore deformation shows a clear variation between active and passive deformation in agreement with the profile of the sensor response. From the illustrative diagram and optical image of the pore deformation during passive compression, the pores start to deform and close during a strain of 45–70%, resulting in little variation in the resistivity. This delay between 0% and 44% suggests that the interconnection between the pores leading to an increase in the conductivity of the overall porous structure changes is only slightly influenced during initial deformation in one direction. Instead, during active actuation, the multidirectional collapse of the pores induced by active vacuum actuation leads to faster pore increase in the conductivity and an immediate and linear sensor response during 15–70% total strain. The suggested mechanism is shown in Figure 1E,F.

Figure 2E is the computed strain plotted against the real measurement of the strain. The data show a linear relationship (error $<15\%$) for strain larger than 22%, whereas for lower compression values the data deviate from the fitting with larger errors (20%). The results are computed using the inverse fitting of strain over $\Delta R/R_0$ ($R^2 = 0.9888$), which is shown in Figure S7B, Supporting Information.

Figure 2F shows the experimental verification of the SFA during concurrent active and passive deformation and how different modes of deformation or compression can be identified and discriminated. The experiment started by a passive deformation of the SFA (PD: only mechanical compression; PD_p: with mechanical compression and positive pressure) using three manually applied asynchronous compressions. The plot shows an average sensor response of $+20\%$ relative resistance when deformed. Later the SFA was switched to active compression (AD: only vacuum; AD_p: with vacuum and positive pressure) controlled by a switch sequence of the electro valves sequentially compressing the actuator, showing an average relative resistance of -79% . The SFA relaxes instantaneously back to the original position

(0%) due to the applied positive pressure, which was used to accelerate the relaxation response of the actuator and, at the same time, to have a clear comparison of the signals when a passive external force was applied while the actuator was moving using the active compression (AD_p). The observed sensor responses show a clearly distinguishable pattern that can be used to analyze the actual source of deformation. In all experiments, we tracked the displacement of the actuator showing the difference between compression or deformation in terms of displacement along the vertical axis as shown in Video S2, Supporting Information.

Compared to actuators with embedded third-party sensing,^[50] the proposed system is a multifunctional device, integrating actuation and sensing into a single component using the intrinsic material functionality of the soft porous composite foams. This makes the SFA versatile, robust, and reliable with straightforward relative resistance measurements that can estimate the current deformation and differentiate between initial active or passive deformation. Table S2, Supporting Information, summarizes the overall characteristics and performance of the average properties of the actuators in various configurations.

2.3. Operational Pressure and Force Characterization/Response of the Actuator

To analyze the load-bearing performance of the SFA, we performed experiments to record its force response. We acquired the force data using a static measurement device while compressing the actuator from its relaxed state to a fixed compression strain, and by pulling it back to the original configuration.

Figure 3A shows the response behavior of the SFA in compression and extension cycles. For the analysis, we plotted the average measured force over ten cycles (blue line in the figure) together with the measurement at each cycle added to the graph (gray dashed line) to better visualize the general force behavior. The very first cycle of the force reading is highlighted as dashed lines to show that the initial force is zero only at the start of the experiment. Figure S8, Supporting Information, shows the force measurements were performed starting from the relaxed position of the actuator at 0 N (A) and by applied vacuum the load cell is pulled which is shown as point A to A'. The linear stage compresses the actuator upto 70% which is point B and pulled back to original length, point C as the actuated position with a

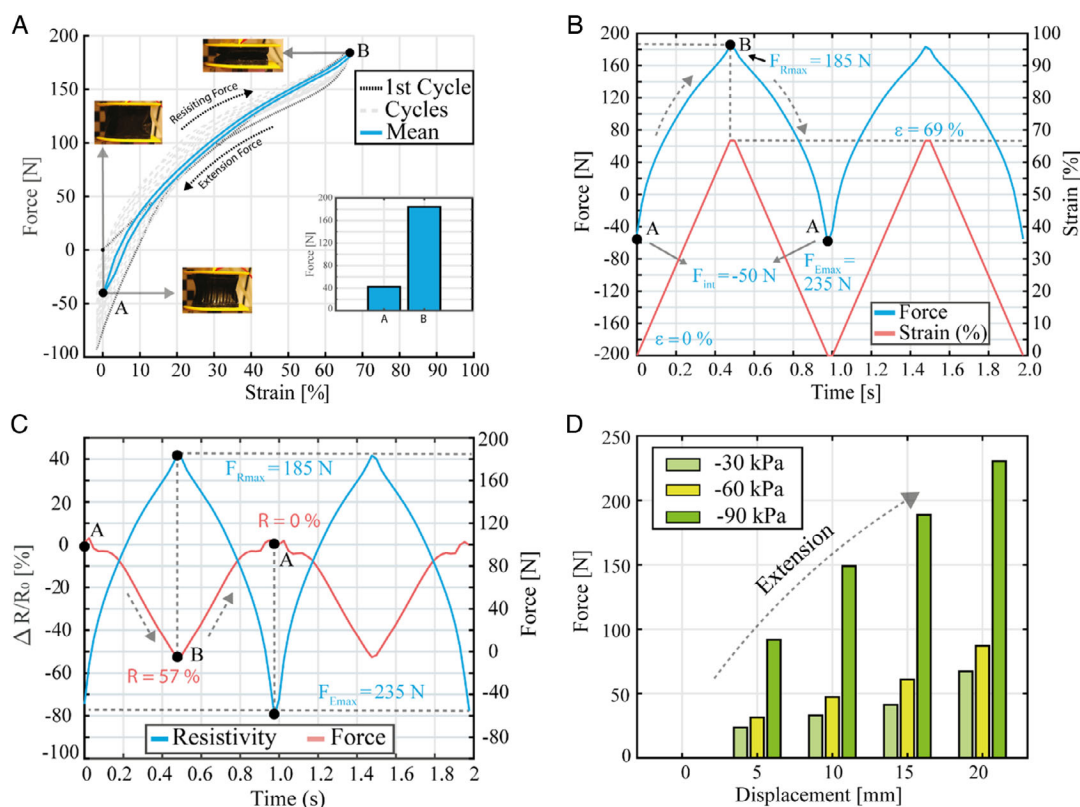


Figure 3. A) Actuation force as a function of the cyclic strain profile during the extension and compression phases of the actuator under a vacuum of -90 kPa. Initial force is zero during the start of the experiment (first cycle) as the linear stage compresses the actuator and simultaneously applying the vacuum shows a resisting force, which jumps to point B (see Figure S8, Supporting Information, for more information). Here, point A to B represents the compression (resisting force) of the actuator and B to A represents the extension phase of the actuator. The small bar graph shows the mean maximum force at points A and B. B) Force and the corresponding strain profile plotted over the time period. C) Resistance change showing the corresponding force response of the actuator plotted over time period. Resistance variation correlates with the force exerted during compression or extension phase of the actuator. D) Tunable stiffness of the actuator by multiple pressure inputs (-30 , -60 , -90 kPa) exhibiting an increase in the force extension profile of the sensorized actuator. At -90 kPa the actuator proves to be stiffer and stronger compared to other pressure values applied. The stiffness index of the actuator is shown in Figure S8, Supporting Information.

resisting force from the applied vacuum. To simplify the process in Figure 3A, the points “A” and “B” are represented as two phases of force response: A is the initial state or extended state; B is the maximum compression phase or resisting force. Values are in means: (A) -50 N is the initial position and force during maximum extension and (B) 185 N is the maximum compression upon actuation, respectively. The actuator can thus withstand a maximum force of 235 N because the actuator returns a maximum force, which is the sum of resisting and initial position forces. This result is due to the fiber-reinforced skin, which prevents the actuator from extending further and ballooning (see Figure S2, Supporting Information; the optical microscopic image shows the alignment of fibers on the fiber-reinforced skin).

To better demonstrate the force behavior, the compression strain and measured forces were analyzed and plotted together over time (Figure 3B). The matching of the force data along the strain profile clearly highlights the reliable and repeatable nature of the actuator. The proprioceptive behavior of the sensor assists in identifying the current state or status of the actuator. Figure 3C shows the correlation between the force measurements and the sensor readings plotted over time. As the plot suggests, the two measurements have a high correlation value, proven by the fact that peaks in both measurements occur instantaneously. The continuous blue line shows the compression force from point A to B and the extension force from point B to A. $\Delta R/R_0$ inversely follows the force curve progression with a minimal resistance variation of 0% during compression, which increases to 57% during the extension phase.

We further evaluated the performance of the actuator during active compression by varying the input pressure from -30 , -60 , up to -90 kPa, and by measuring the forces exerted at an equal interval of displacement during compression and extension. Figure 3D summarizes the results by taking the average mean of the complete extension phase. The values represent the maximum forces obtained as the sum of resisting and initial position forces. With -30 kPa as the initial input pressure, the actuator exerts less force and thus easily follows the movements induced by the testing platform. When the input pressure is increased to -60 kPa, the force of the actuator also increases during its extension phase. The actuator moves from compressed to relaxed configurations as a consequence of the increased force. When the input pressure is increased to -90 kPa, the maximum force of the actuator is where it can withstand a maximum load of 24 kg (≈ 235 N). At the same time, by applying different input pressures, the SFA showed variable stiffness properties such as the stiffness factor (k), which demonstrated increased strength over strain length, as shown in Figure S8, Supporting Information. See Table S2, Supporting Information, for actuator performance and physical parameters. Video S3, Supporting Information, shows the characterization and performance of the actuator.

3. Sensorized Soft Robots from Reconfigurable Modules

Modular sensorized actuators can be easily integrated into a variety of soft robots due to their design and task flexibility. Figure S9, Supporting Information, shows three soft robotic systems, specifically 1) a soft compression piston-like actuator,

2) a gait-pattern-controlled inchworm-like crawling locomotion, and 3) a robotic trunk-like manipulator. We validated the distinct functionalities facilitated by these modules by demonstrating the robot behavior in its environment as an example for the perception of the robot's status.

3.1. Soft Compression Piston-Like Actuator

As the proposed SFA can exert a high force, it can be used to move loads and hold them in position. The initial testing indicated that the compliance of the actuator does not significantly affect repeatability. Variable compressibility was identified using a different applied load achieved by applied input pressure. This was apparent from qualitative observations of the load-lifting tasks performed by the SFA. Although the actuator is made of soft materials, it is sufficiently robust and stiff to maintain positioning and to follow the motion.

Figure 4A shows time-lapse snapshots of the conductive piston-like actuator, which consists of a module containing a single actuator that can carry different loads. The actuator and the actuation sequence are shown in Figure 4B,C, respectively. In this task, the actuator is fixed at one end, while different loads are mechanically attached to the other end using a 3D-printed hanger. The tests were performed starting with no load and sequentially adding loads up to 6 kg. For each load, ten cycles were performed with a time delay of 8 s between the compressed and relaxed state operated with both positive (40 kPa) and negative pressure (-90 kPa). Figure 4D shows that $\Delta R/R_0$ decreases from 84% without a load to 29% for the maximum load (6 kg). The compression and extension phase of the soft piston-like actuator is shown in the zoomed-in version with a colored background. The overshoot above zero is due to the effect of the positive pressure and the pulling effect of the applied load. Video S5, Supporting Information, shows the actuator pulling different loads.

3.2. Inchworm-Like Crawling Locomotion

Inchworm-like crawling locomotion can be achieved using the proposed actuator as a sensorized module integrated into a modular robot. Crawling enables rapid locomotion typically over wide open terrains using a high-frequency crawling gait, on the slower frictional surface. By sensing the changes in the actuation pattern due to actuator deformations, the robot's locomotion behavior showed a response during the compression and forward motion for every single module of the robot. A time-lapse image of the crawling locomotion with a forward gait locomotion sequence is shown in Figure 5A.

To further prove the SFA's functionalities, we assembled six modules (each containing a single SFA) in series and actuated them in sequence to achieve a wave-like crawling locomotion. Figure 5B shows a sequence of the forward wave gait over a flat surface with a speed of 5 mm s^{-1} (0.05 body length (BL) s^{-1}). The speed can be varied by increasing or decreasing the actuation frequency. The crawling locomotion of the robot can be detected by the foam sensor as a binary switch modulated on a sinusoidal gait pattern. Figure 5C shows the sensor response acquired by the head, the tail, and the midunit module, ranging from 20% to 40% in relative resistance between the compressed and relaxed

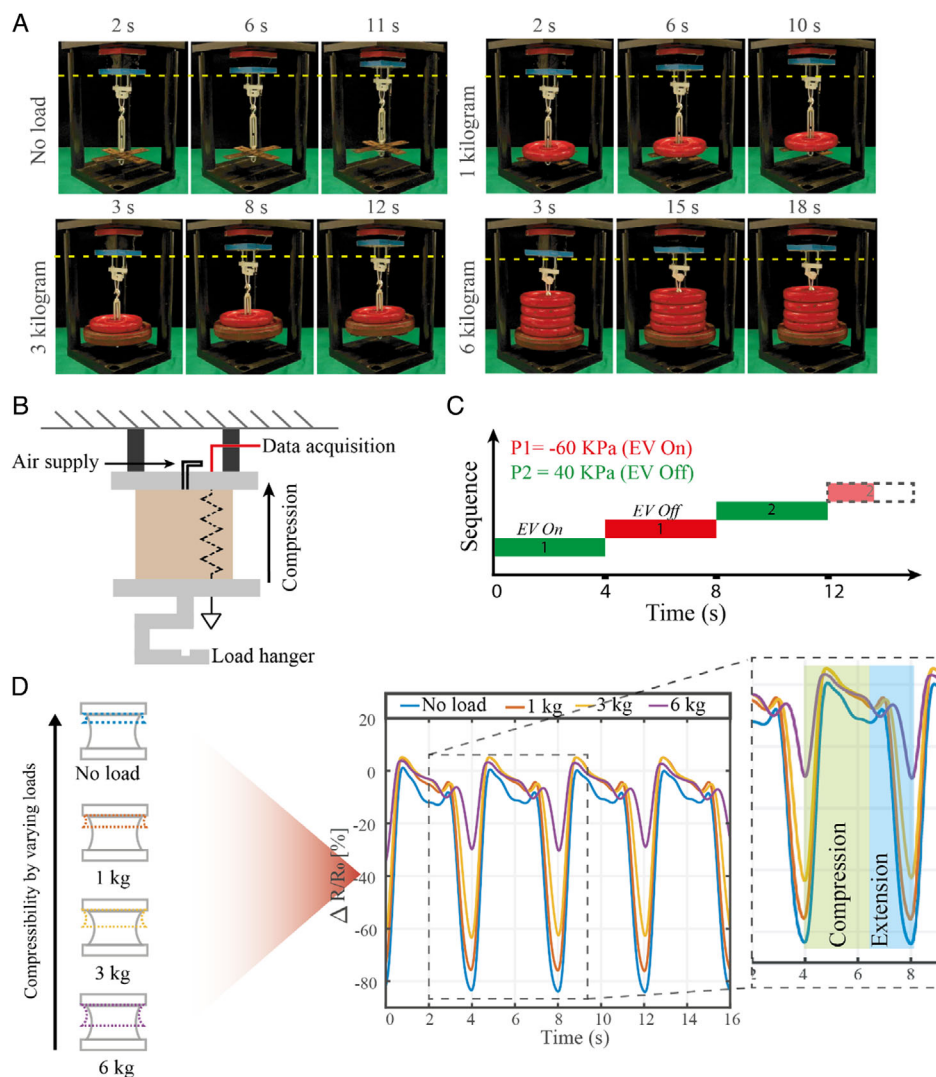


Figure 4. A) SFA lifting different weights from 0 to 6 kg. The yellow dashed line indicates the position of the actuator in the relaxed state. B) The soft weight-pulling piston-like actuator with a load/weight hanger. C) Electrovalve control sequence of the actuator (top) and the difference in compression strain percentage achieved as a function of the applied load/weight (bottom). D) Relative resistance changes as a function of time and applied load. The zoomed-in plot highlights the compression and extension phases, showing the difference in relative resistance by varying the applied load, which affects the compression strain.

phase. The compression and extension phase of the actuator is highlighted with color strips. Although the actuators perform at full compression, the high operation speed prevents the foam from returning to its complete relaxed state and the sensing is thus limited. However, this issue can easily be overcome by acquiring the data during an initial cycle of locomotion and then using this as a reference for the full range of compression. Video S6, Supporting Information, shows the results of the robot's inchworm-like crawling locomotion.

3.3. Modular Trunk-Like Manipulator

We also tested the ability of the actuator to work both in series and in parallel configurations. In this case, each module consists of three SFAs that are placed in a 120° configuration (Figure 5D),

enabling the module to perform three basic motions: 1) compression, 2) extension, and 3) rotation. By stacking these modules in series, we assembled a robotic trunk-like manipulator, which has one end fixed to a stationary base and the other end has a load hanger. By sequentially activating each of the SFAs along the same direction (e.g., all the actuators placed at 0°, or all the actuators placed at 120°), we can achieve 360° motion.

In this test, we used the sensing capability to evaluate how well the manipulator detects the presence of an applied load and then adapts its motion accordingly. We selected sensorized module 1 and module 4 (Figure 5F) and qualitatively evaluated the influence of the active components (actuated) on the adjacent passive components (nonactuated) for each module.

As shown in Figure 5, the actuation sequence and readings of the sensors can be clearly subdivided into three main zones:

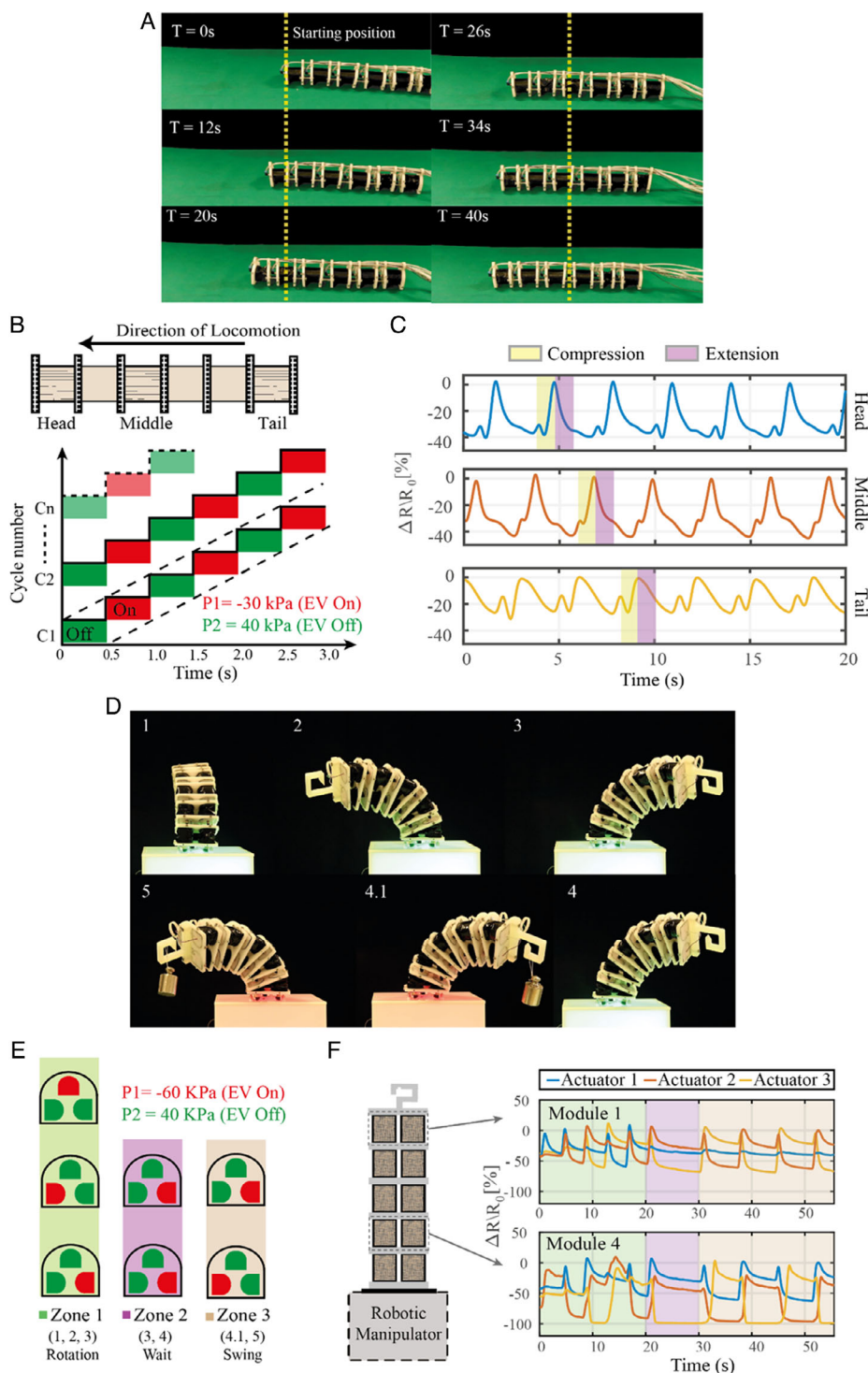


Figure 5. A) Time-lapse images of inchworm-like crawling locomotion using sensorized soft actuator modules (see Video S5, Supporting Information, on locomotion experiment). B) Gait pattern to sequentially activate the actuator modules for forward and backward locomotion (top) and illustration (bottom) of the actuator modules highlighting the sensorized ones used to acquire the information on active and passive deformation. The sensorized modules are: head (1), middle (3), and tail (6). C) Three different plots with relative resistance change as a function of time representing the locomotion behavior of the actuator modules, exhibiting the compression (green) and extension (purple) phases during the locomotion scenario. D) Time-lapse images of robotic trunk-like manipulator using the sensorized soft actuator modules. E) Activation sequence to manipulate the carrying load with different zones for enabling three different behaviors such as 360° rotation, stationed wait time, followed by swing motion. F) Illustration of the robotic manipulator and the modules activated to monitor the manipulation task. The plot shows the sensor data for three different actuations of the manipulator within the zone sequence showing a difference in behavior.

1) 360° rotation (zone 1), 2) waiting-time (zone 2), and 3) swing motion (zone 3). After two cycles of complete rotation (zone 1), all the sensors facing the front-right direction (yellow line) detected a compression between 20 and 30 s (zone 2) due to an applied load of 400 g. As a consequence, the motion pattern changed to swing motion (zone 3) until the load was removed.

The change in the compression pattern of the modules due to an external load is further indicated by a change in the lighting color of the base platform (green: no load, red: with load), which changes again when the load is removed in response to the sensor readings. Video S7, Supporting Information, shows the experiment in detail.

4. Discussion

There is a clear demand for integrable actuation and sensing solutions in soft robotics, which are particularly useful when robots have to interact safely with living creatures, or delicate objects in unstructured environments.^[49–53] Such functionality can be incorporated by tuning and using material functionality. The SFA presented here consists of a functionalized conductive foam core that detects its own deformation and, consequently, its motion in the surroundings. Compared to other pneumatic actuators,^[54] using a rapid manufacturing solution eliminates complex molding techniques and enables batch production with minimal effort.

The modular design of the integrable SFAs facilitates a reconfigurable assembly into soft modular robots. **Table 1** compares the response time, load capacity, and sensing with other recently developed pneumatic soft actuators. The values reported are considered as the best-case scenario for all actuators—the performance might change by applying different loads or by changing the actuator configuration. The comparison indicates that our actuator shows fast response with a higher load-withstanding capacity with integrated reconfigurable modules and intrinsic proprioceptive responses.

Although elastomeric actuators are considered the state of the art for soft robotic applications, they are limited by the low

actuation cycle and effective use of the actuation source. Due to the support components, the SFA lasts for more than 10 000 continuous cycles, whereas similar elastomeric actuators exert less force and can typically only last for a few cycles.

The results in Figure 1E show that during passive compression, the actuator first exhibits an increase in the relative resistivity ($\Delta R/R_0$), which is then followed by a linear decrease up to its maximum compression (70% strain). In contrast, during active compression, the trend of $\Delta R/R_0$ is linear and consistent and the hysteresis is less than 4%. This particular behavior is due to the porosity deformation of the material itself caused by the opening and closing of the porous walls, as explained in Figure 1E–G. The low hysteresis of the SFAs enables the compressive strain corresponding to the $\Delta R/R_0$ to be detected, as shown in Figure 2D. Figure 2F shows the observed sensor responses can clearly distinguish pattern that can be used to analyze the actual source of deformation. In all experiments, we tracked the displacement of the actuator showing the difference between compression and deformation in terms of displacement along the vertical axis, as shown in Video S2, Supporting Information.

Figure 3 show the results of the high extension force achieved upon actuation, which can be predicted with the corresponding strain percentage. By varying the input pressure, the actuator stiffness or the resisting force is tuned to withstand a maximum load of 24 kg. The same stiffness variation takes place by applying different loads in the compression soft piston-like motion. This was possible using the 100 μm thin polyethylene film used as reinforced skin, which reduces the effect of inflation or ballooning, and enables the actuator to use both positive and negative pressure as an input to the actuators. This prevents damaging the actuator and helps to improve performance, which is typical when elastomeric-based materials are used. In addition, both positive and negative pressure can be combined to provide forces greater than one order of magnitude compared to current actuators.

Figure S3, Supporting Information, highlights that the use of both positive and negative pressure ensures a faster and smoother response, and regulates the stiffening of the actuator,

Table 1. Comparison of the response time and load capacity of compression-based soft pneumatic actuators with integrated sensor.

	Response time [s]		Load capacity [N]	Sensing	Actuation (P/N/both) ^{a)}	Year
	Actuation	Relaxation				
This work (CFA)	1.65	1.35	235	Resistivity	P/N	2021
Tang et al. ^[58]	1.26	2.60	3.4	–	P	2020
Jiao et al. ^[59]	0.47	0.67	88.2	–	N	2018
Yang et al. ^[60]	0.6	–	4.96	–	N	2016
Robertson et al. ^[55]	1.5	2.4	3.7	–	N	2017
Benjamin et al. ^[45]	–	–	20	–	N	2015
Li et al. ^[61]	–	–	200	–	P/N	2017
Tawk et al. ^[62]	0.10	0.5	27	–	N	2019
Sonar et al. ^[63]	0.03	0.02	10	PZT	P	2016
Veale et al. ^[64]	0.05	–	40	–	P	2016
Zhou et al. ^[65]	5	5	24.9	Resistivity	P/N	2020

^{a)}P: positive pressure; N: negative pressure.

and thus tunes the force exerted. This improves the response behavior to ensure a stable motion of the actuator and prevents the wrinkles on the fiber-reinforced skin during the relaxation phase.

In this article, we mainly focused on a deformation behavior for SFA characterization, which is a good fit for the soft robotics applications presented here. This was demonstrated by various systems, such as the compression soft piston-like actuator, crawling locomotion module, and robotic trunk-like manipulator. Figure 4 and 5 show possible applications and highlight the versatility of the SFA and how the change in relative resistance, the force exerted over time, and the strain percentage can be used to study the behavioral change of a soft robot.

However, as shown in Video S7, Supporting Information, the mechanical constraint between adjacent actuators might reduce the mobility of the SFA. More effective methods of stacking the modules could be implemented to maintain the robot's efficient operation. From the results shown in Figure 2F, the actuator produces a distinct response when actively compressed or passively deformed. These changes allow us to easily discriminate between these two types of compression by considering the following three main factors: first, by the time response of the actuator during passive deformation showing random time periods compared to active deformation as determined by the control sequence of the electro valves. Second, the profile of the relative resistance change correlating to different pore deformation dynamics enables us to detect the change in motion when SFAs are actively actuated by vacuum or passively deformed by external forces. Third is by monitoring the compression strain of the actuator, which could clearly discriminate between active and passive compression. This suggests a clear potential to identify and distinguish multiple forces affecting the actuator. Using such information as a set point to the control identifier may allow the soft robotic system to obtain better adaptation and control in unstructured environments. Our future works aim to achieve such adaptation to realize the system in physical world scenarios.

In the future, the performance and number of applications could be increased with a decentralized design and a feedback-based control system with autonomous control, and deep learning techniques for multiterrain locomotion, as well as a fully functional modular platform in addition to a higher softness index of the actuator.

Because the robot is currently driven by an external pneumatic pump, its propulsion system is bulky, especially compared with other modular robots.^[55] In fact, a fully contained soft robot driven by a pneumatic system could house miniature pneumatic diaphragm pumps, an electrovalve, microcontroller, sensor, and an in-house battery, which could be organized in a closed modular chamber, rather than built externally.

5. Conclusion

The modular and reconfigurable SFAs presented here are straightforward to manufacture with feature-tunable actuation modes. The SFAs can be designed to tune their stiffness, perform compression and extension motion, and be arranged in different configurations. In addition, the integrated sensing can monitor active compression modes as well as passive

deformation, thus providing versatile self-sensing enabled by the intrinsic material properties. The characteristic pore shape evolution during active and passive compression of the SFA especially enhances the sensing, adaptability, and accuracy of the system, and the fiber-reinforced encapsulation facilitates excellent soft actuation with high load-withstanding capacity and versatile integrability. Our SFA provides an easy-to-implement, fast, precise, adaptable, and modular actuation and sensing unit which can be used to create a variety of soft robotic scenarios.

6. Experimental Section

Preparation of the Conductive Ink: The synthesis of the conductive ink is adapted from a previous study.^[56] A total of 1.0 g of carbon black nanoparticles (Cabot Inc., Vulcan XC-72) having a bulk density of 96 kg m^{-3} (6 lbs ft^{-3}) and an average particle size of 50 nm ^[57] was dispersed into 16 mL of 2-propanol solution in a 50 mL vial and sonicated for 15 min. In another 50 mL vial, 4.0 g of prepolymer (Smooth-ON Inc., Ecoflex 00-50) was dissolved in 18 g toluene (Sigma Aldrich). The solution was stirred until the silicone was completely dissolved. The carbon mixture and the silicone solution were then mixed and stirred for 15 min with a magnetic stirrer to obtain the final ink. During the preparation of the conductive ink, the prepolymer mixture cross-links, acting as a matrix for the conductive carbon particles without completely coating and isolating the single particles as expected by the observed conductivity.

Soft and open porous foam (Modulor GmbH, Germany, Item no 0333035) was wire-cut into a desired shape and immersed into the bath of conductive ink. During immersion, a gentle force was applied from the top and bottom using flat plates to remove the excess ink and trapped air from the pores. This "dip-and-squeeze" step was repeated three times. The coated foam was dried at room temperature, 25°C , for 30 min and then kept inside the oven at 110°C for 60 min, where it retained its original shape and the solvent evaporated. Figure S1, Supporting Information, explains the whole process involved in the preparation of the conductive foam. To assess the average thickness of the conductive coating layer, a sample was sliced and observed under a scanning electron microscope (SEM, Dual Beam FIB, Helios HVI36), revealing an average thickness of $\approx 4.29 \pm 0.5 \mu\text{m}$ (see Figure S2A, Supporting Information, for scanning electron microscopy and Figure S2B, Supporting Information, for the microanalysis of the conductive foam).

Actuation Design and Manufacturing: The manufacturing process of the SFA (Figure S1, Supporting Information) begins with the design of the frame of the actuator, which is made of delrin (POM) using a 2D laser cutter (Universal Laser System, VLS 3.0). This frame acts as a support. The sensorized foam core acts as an internal scaffold, and was cut using a nickel wire cutter (customized machine). The components selected for manufacturing are shown in the Table ST1, Supporting Information. The sensorized form core was connected to the frame by gluing two thin copper layers together (0.3 mm), which act as an electrode when spread with a thin layer of conductive silver epoxy (Chemtronics, CW2400). The masked film was then placed over the foam core, interlaying a sheet of paper as an inextensible layer between the foam and the fiber-reinforced polyethylene (PE) film. This thus prevents wrinkles on the fiber-reinforced skin, which acts as sealing layer around the foam.

This creates an enclosed, airtight structure that is only sparsely filled with soft, porous conductive foam. The fiber-reinforced skin helps to build a stronger actuator, thus enabling a fast response. This skin exerts a strong force, whereas a stretchable elastomeric skin could have weakened the strength of the actuator (Figure S2, Supporting Information, provides optical imaging details of the fiber-reinforced skin with the fiber arrangement).

The support frame is used to host electrical and pneumatic connections to ensure that only the conductive foam is compressed/extended during its operating time. Foam with a fixed width of 30 mm was used, and its length and height varied due to the different shapes used. The actuator can also be batch manufactured with different sizes and shapes.

Demonstration of Sensor Robustness and Resilience: To ensure the repeatability and consistency in the measurements, a Universal Testing Machine (Z005, Zwick/Roell) was used to apply an initial preload, and to ensure precise vertical movements. This device comes with a load cell attached (Xforce-P, 1 kN, Zwick/Roell) to measure the force exerted by the actuator during compression and extension. Then the measurements were repeated by varying the different actuation modalities for 11 cycles. The input pressure was varied by switching between a positive supply to a vacuum source using an electrovalve gate (TX-3-P006, First Sensor). See Figure 4 and 5, Supporting Information, for details on the experimental setup and instrumentation.

Concurrent Experimental Verification: For concurrent active and passive stimulation as given in Figure 2F, the actuator was placed on a fixed plate and the experiment started with passive deformation by three asynchronous compressions applied by manually pressing the actuator. Then, the same was conducted under an applied positive pressure for faster relaxation. Subsequently, the SFAs were switched to active compression with an applied vacuum of -90 kPa, leading to immediate compression of the actuator as during typical actuation. Between every experiment, an actuator relaxation time of $\approx 5-10$ s was fixed. The sensor response as a function of the different deformations was recorded.

Time Response of the Actuator in Different Modes: The performance of the actuators was tested by comparing the compression modes: passive or active. In this subsection, the relaxation time is focused on. The active compression is extended by considering two different relaxation modes. In mode 1, the decompression is performed by enabling the foam to recover its original shape using atmospheric pressure. In mode 2, the recovery is performed by pressurizing the actuator with a positive pressure of 40 kPa. In both modes, the compression phase remains the same as before. Video S4, Supporting Information, shows the response of the actuator during the two actuation modes, and Figure S3, Supporting Information, shows the different actuation modes of the SFA.

Figure S3, Supporting Information, highlights that the speed of recovery time was shortened considerably from on average $3.71-13.3$ mm s $^{-1}$, which is five times faster and is more controllable (the dashed area in the Figure S3, Supporting Information, shows an unstable relaxation during mode 1). The two methods are comparable only when the actuator is covered with the external skin because this enables the compression of the actuator. When there is no skin, the only actuation possible is the one induced passively by external forces. By tuning between different modes of actuation, the SFA can vary its stiffness or force behavior.

Measurement and Data Analysis: The sensor electrical resistance was acquired using a National Instruments DAQ card NI-USB 6216 to which the SFA was connected, in a voltage divider configuration with a constant resistance of 100 k Ω (with $<1\%$ accuracy). Displacement data, measured forces, and cycle number were collected directly by a static measurement device (Z005, Zwick/Roell). To ensure correspondence between the data timestamps, the measurements were taken from the same computer.

For each of the experiments, data for 11 cycles (10 + 1) were acquired and the first cycle was not considered to ensure consistency. The data were then averaged by cycle, or by distance traveled (i.e., by grouping the distance into bins of fixed length). Regarding the performance results of the two actuation modes (i.e., active and passive compression), analyses were performed by optically tracking markers placed on the actuator, and by averaging the time required from full compression to full relaxation.

Supporting Information

Supporting Information is available from the Wiley Online Library or from the author.

Acknowledgements

The references [7], [10], [12] and [23] were amended on June 22, 2021, after initial publication online. The authors thank Carlo Filippeschi for performing dual beam (SEM) imaging and microanalysis of the conductive foam.

The Supporting Information of this article can be found here: <https://doi.org/10.1002/aisy.202100022>.

Conflict of Interest

The authors declare no conflict of interest.

Data Availability Statement

Research data are not shared.

Keywords

integrated design, porous materials, proprioception, soft actuators and sensors, soft robotic applications, variable stiffness

Received: February 2, 2021

Revised: March 12, 2021

Published online: May 18, 2021

- [1] R. Pfeifer, M. Lungarella, F. Iida, *Commun. ACM* **2012**, *55*, 76.
- [2] R. Pfeifer, M. Lungarella, F. Iida, *Science* **2007**, *318*, 1088.
- [3] B. Mazzolai, C. Laschi, *Sci. Robot.* **2020**, *5*, 1.
- [4] D. Rus, M. T. Tolley, *Nature* **2015**, *521*, 467.
- [5] A. A. Stokes, R. F. Shepherd, S. A. Morin, F. Iliovski, G. M. Whitesides, *Soft Robot.* **2014**, *1*, 70.
- [6] J. Rossiter, H. Hauser, *IEEE Robot. Autom. Mag.* **2016**, *23*, 17.
- [7] S. P. Murali Babu, A. Sadeghi, A. Mondini, B. Mazzolai, "Preliminary Study on Locomotion Performance of WaveBot on Different Surfaces Using Traveling Waves," *9th International Symposium on Adaptive Motion of Animals and Machines (AMAM 2019) PP - EPFL*, Lausanne, Switzerland. doi: 10.5075/epfl-BIOROB-AMAM2019-60.
- [8] B. S. Homborg, R. K. Katzschnmann, M. R. Dogar, D. Rus, *IEEE Int. Conf. Intell. Robot. Syst.* **2015**, *2015*, 1698.
- [9] A. Sadeghi, A. Mondini, B. Mazzolai, *Actuators* **2019**, *8*, 47.
- [10] S. P. M. Babu, A. Sadeghi, A. Mondini, B. Mazzolai, "Antagonistic pneumatic actuators with variable stiffness for soft robotic applications," *RoboSoft 2019 - 2019 IEEE Int. Conf. Soft Robot.*, **2019**, pp. 283-288, doi: 10.1109/ROBOSOFT.2019.8722803.
- [11] M. D. Grissom, V. Chitrakaran, D. Dianno, M. Csencits, M. Pritts, B. Jones, W. McMahan, D. Dawson, C. Rahn, I. Walker, in *Proc. of SPIE, The International Society for Optical Engineering*, Kissimmee, FL, USA **2006**, p. 62301F.
- [12] M. Cianchetti, T. Ranzani, G. Gerboni, I. De Falco, C. Laschi, A. Menciassi, "STIFF-FLOP surgical manipulator: Mechanical design and experimental characterization of the single module," *IEEE Int. Conf. Intell. Robot. Syst.*, **2013**, pp. 3576-3581, doi: 10.1109/IROS.2013.6696866.
- [13] M. T. Tolley, R. F. Shepherd, B. Mosadegh, K. C. Galloway, M. Wehner, M. Karpelson, R. J. Wood, G. M. Whitesides, *Soft Robot.* **2014**, *1*, 213.
- [14] M. W. Hannan, I. D. Walker, *J. Robot. Syst.* **2003**, *20*, 45.
- [15] M. Cianchetti, A. Arienti, M. Follador, B. Mazzolai, P. Dario, C. Laschi, *Mater. Sci. Eng. C* **2011**, *31*, 1230.
- [16] S. Taccola, F. Greco, E. Sinibaldi, A. Mondini, B. Mazzolai, V. Mattoli, *Adv. Mater.* **2015**, *27*, 1668.
- [17] A. S. Kuenstler, R. C. Hayward, *Curr. Opin. Colloid Interface Sci.* **2019**, *40*, 70.
- [18] M. Behl, K. Kratz, U. Noechel, T. Sauter, A. Lendlein, *Proc. Natl. Acad. Sci.* **2013**, *110*, 12555.

- [19] F. Meder, G. A. Naselli, A. Sadeghi, B. Mazzolai, *Adv. Mater.* **2019**, 31.
- [20] G. K. Klute, J. M. Czerniecki, B. Hannaford, in *IEEE/ASME Int. Conf. Adv. Intell. Mechatronics*, AIM, Atlanta, GA, USA **1999**, p. 221.
- [21] V. Vikas, E. Cohen, R. Grassi, C. Sozer, B. Trimmer, *IEEE Trans. Robot.* **2016**, 32, 949.
- [22] M. Wei, Y. Gao, X. Li, M. J. Serpe, *Polym. Chem.* **2017**, 8, 127.
- [23] C. Della Santina, R. K. Katzschmann, A. Bicchi, D. Rus, "Dynamic control of soft robots interacting with the environment," *2018 IEEE Int. Conf. Soft Robot. RoboSft 2018*, **2018**, pp. 46–53, doi: 10.1109/ROBOSOFT.2018.8404895.
- [24] E. Di Paolo, in *Organismically-Inspired Robotics: Homeostatic Adaptation and Teleology Beyond the Closed Sensorimotor Loop*, Advanced Knowledge International, Adelaide, Australia **2003**, p. 19.
- [25] S. K. Mitchell, X. Wang, E. Acome, T. Martin, K. Ly, N. Kellaris, V. G. Venkata, C. Keplinger, *Adv. Sci.* **2019**, 6, 1900178.
- [26] R. K. Katzschmann, A. D. Marchese, D. Rus, *Soft Robot.* **2015**, 2, 155.
- [27] J. C. Yeo, H. K. Yap, W. Xi, Z. Wang, C. H. Yeow, C. T. Lim, *Adv. Mater. Technol.* **2016**, 1, 1.
- [28] S. S. Robinson, K. W. O'Brien, H. Zhao, B. N. Peele, C. M. Larson, B. C. Mac Murray, I. M. Van Meerbeek, S. N. Dunham, R. F. Shepherd, *Extrem. Mech. Lett.* **2015**, 5, 47.
- [29] P. Polygerinos, N. Correll, S. A. Morin, B. Mosadegh, C. D. Onal, K. Petersen, M. Cianchetti, M. T. Tolley, R. F. Shepherd, *Adv. Eng. Mater.* **2017**, 19, 1700016.
- [30] A. Sadeghi, A. Mondini, M. Totaro, B. Mazzolai, L. Beccai, *Adv. Eng. Mater.* **2019**, 21, 1.
- [31] T. Yano, S. Fujimoto, T. Akagi, W. Kobayashi, *Int. J. Mech. Eng. Robot. Res.* **2020**, 9, 190.
- [32] K. Omura, K. Goto, S. Wakimoto, T. Kanda, in *ACTUATOR 2018; 16th Int. Conf. New Actuators*, VDE Verlag GmbH, Germany **2018**, pp. 1–4.
- [33] S. P. Murali Babu, F. Visentin, A. Sadeghi, A. Mondini, B. Mazzolai, *IEEE Robot. Autom. Lett.* **2020**, 3766, 1.
- [34] C. Larson, B. Peele, S. Li, S. Robinson, M. Totaro, L. Beccai, B. Mazzolai, R. Shepherd, *Science* **2016**, 351, 1071.
- [35] L. N. Awad, J. Bae, K. O'Donnell, S. M. M. De Rossi, K. Hendron, L. H. Sloom, P. Kudzia, S. Allen, K. G. Holt, T. D. Ellis, C. J. Walsh, *Sci. Transl. Med.* **2017**, 9.
- [36] Z. Erickson, M. Collier, A. Kapusta, C. C. Kemp, *IEEE Robot. Autom. Lett.* **2018**, 3, 2245.
- [37] G. Soter, A. Conn, H. Hauser, J. Rossiter, in *Proc. – IEEE Int. Conf. Robot. Autom.*, IEEE, Brisbane, Australia **2018**, pp. 2448–2453.
- [38] H. Liu, Q. Li, S. Zhang, R. Yin, X. Liu, Y. He, K. Dai, C. Shan, J. Guo, C. Liu, C. Shen, X. Wang, N. Wang, Z. Wang, R. Wei, Z. Guo, *J. Mater. Chem. C* **2018**, 6, 12121.
- [39] A. Atalay, V. Sanchez, O. Atalay, D. M. Vogt, F. Haufe, R. J. Wood, C. J. Walsh, *Adv. Mater. Technol.* **2017**, 2, 1.
- [40] L. Y. Xu, G. Y. Yang, H. Y. Jing, J. Wei, Y. D. Han, *Nanotechnology* **2014**, 25.
- [41] A. Fassler, C. Majidi, *Adv. Mater.* **2015**, 27, 1928.
- [42] S. Gong, D. T. H. Lai, Y. Wang, L. W. Yap, K. J. Si, Q. Shi, N. N. Jason, T. Sridhar, H. Uddin, W. Cheng, *ACS Appl. Mater. Interfaces* **2015**, 7, 19700.
- [43] C. Choi, W. Schwarting, J. Delpreto, D. Rus, *IEEE Robot. Autom. Lett.* **2018**, 3, 2370.
- [44] J. Ulmen, M. Cutkosky, in *Proc. – IEEE Int. Conf. Robot. Autom.*, IEEE, Anchorage, AK, USA **2010**, pp. 4836–4841.
- [45] B. C. Mac Murray, X. An, S. S. Robinson, I. M. Van Meerbeek, K. W. O'Brien, H. Zhao, R. F. Shepherd, *Adv. Mater.* **2015**, 27, 6334.
- [46] B. C. Mac Murray, C. C. Futran, J. Lee, K. W. O'Brien, A. A. Amiri Moghadam, B. Mosadegh, M. N. Silberstein, J. K. Min, R. F. Shepherd, *Soft Robot.* **2018**, 5, 99.
- [47] E. J. Garboczi, D. P. Bentz, N. S. Martys, *Digital Images Comput. Model.* **1999**, 35, 1.
- [48] M. Su, R. Xie, Y. Zhang, X. Kang, D. Huang, Y. Guan, H. Zhu, *Appl. Sci.* **2019**, 9, 1.
- [49] A. Rafsanjani, Y. Zhang, B. Liu, S. M. Rubinstein, K. Bertoldi, *Sci. Robot.* **2018**, 3, eaar7555.
- [50] T. G. Thuruthel, B. Shih, C. Laschi, M. T. Tolley, *Sci. Robot.* **2019**, 4, eaav1488.
- [51] K. C. Galloway, K. P. Becker, B. Phillips, J. Kirby, S. Licht, D. Tchernov, R. J. Wood, D. F. Gruber, *Soft Robot.* **2016**, 3, 23.
- [52] A. Sadeghi, E. Del Dottore, A. Mondini, B. Mazzolai, *Soft Robot.* **2020**, 7, 85.
- [53] W. Friedl, M. A. Roa, *Front. Robot. AI* **2020**, 6, 1.
- [54] R. F. Shepherd, F. Ilievski, W. Choi, S. A. Morin, A. A. Stokes, A. D. Mazzeo, X. Chen, M. Wang, G. M. Whitesides, *Proc. Natl. Acad. Sci.* **2011**, 108, 20400.
- [55] M. A. Robertson, J. Paik, *Sci. Robot.* **2017**, 2, 1.
- [56] Y. Liu, F. Li, Q. Xia, J. Wu, J. Liu, M. Huang, J. Xie, *Nanoscale* **2018**, 10, 4771.
- [57] Z. Y. Liu, J. L. Zhang, P. T. Yu, J. X. Zhang, R. Makharia, K. L. More, E. A. Stach, *J. Electrochem. Soc.* **2010**, 157, B906.
- [58] Y. Tang, Y. Chi, J. Sun, T. H. Huang, O. H. Maghsoudi, A. Spence, J. Zhao, H. Su, J. Yin, *Sci. Adv.* **2020**, 6, aaz6912.
- [59] Z. Jiao, C. Ji, J. Zou, H. Yang, M. Pan, *Adv. Mater. Technol.* **2019**, 4, 1.
- [60] D. Yang, M. S. Verma, J. H. So, B. Mosadegh, C. Keplinger, B. Lee, F. Khashai, E. Lossner, Z. Suo, G. M. Whitesides, *Adv. Mater. Technol.* **2016**, 1, 31.
- [61] S. Li, D. M. Vogt, D. Rus, R. J. Wood, *Proc. Natl. Acad. Sci.* **2017**, 114, 13132.
- [62] C. Tawk, G. M. Spinks, M. In het Panhuis, G. Alici, in *IEEE/ASME Int. Conf. Adv. Intell. Mechatronics*, AIM, Hong Kong, China **2019**, p. 50.
- [63] H. A. Sonar, J. Paik, *Front. Robot. AI* **2016**, 2, 1.
- [64] A. J. Veale, S. Q. Xie, I. A. Anderson, *Smart Mater. Struct.* **2016**, 25.
- [65] J. Zhou, Y. Chen, X. Chen, Z. Wang, Y. Li, Y. Liu, *IEEE Robot. Autom. Lett.* **2020**, 5, 1867.